Transition from the Layered Sr_2RhO_4 to the Monodimensional Sr_4RhO_6 Phase

Aurea Varela,[a, c] Khalid Boulahya,[a] Marina Parras,[a] José M. González-Calbet,*[a] Thomas Vogt,[b] and Douglas J. Buttrey[c]

Abstract: Study of the structural changes occurring during the reduction process of the $Sr_2RhO_{4+\delta}$ (214), $n=1$ term of the Ruddlesden and Popper series, shows that for $\delta < 0.02$ values, this material dissociates into the Sr_4RhO_6 (416) monodimensional phase, $\alpha=\infty$, $\beta=0$ compound of the $(A_3B_2O_6)_\alpha$-$(A_3B_3O_9)_\beta$ family, and Rh metal. During the first stage, this process occurs by the formation of an intergrowth between the (214) and (416) materials which can be only detected by high resolution electron microscopy and is easily interpreted on the basis of the structural relationship established between them. Further reduction allows the segregation of both phases as separated entities, which coexist with Rh metal. The dissociation process is reversible and, under oxidizing conditions, a layered material with anionic composition $\delta=0.06$ is always obtained. This behaviour seems to be a general way of accommodating the compositional changes in layered A_2BO_4 phases where the B cation is always in a octahedral environment. The structural mechanism of this transformation is proposed, and the structural relationship between these two low-dimensional oxides is established.

Keywords: electron diffraction · electron microscopy · oxides · solid-state chemistry

Introduction

A large number of oxide compounds which structures can be derived from cubic or hexagonal perovskite has been widely studied and reported. Among them, particular attention has been devoted to low-dimensional oxides, both one and two dimensional, due to their interesting structural and physical properties.

In this sense, much work has been done on the layered $A_{n+1}B_nO_{3n+1}$ Ruddlesden and Popper phases. The basic units comprising their crystal structures are $[BO_6]$ octahedra linked by corners to form $(ABO_3)_n$ cubic perovskite layers. These blocks are separated by a rock-salt AO-type layer, leading to quasi-two-dimensional solids. When $n=1$, one cubic block of perovskite alternates with one AO layer along the crystallographic c direction; this results in the K_2NiF_4 structure, which crystallizes in the tetragonal $I4/mmm$ space group (depicted in Figure 1a), although related phases can distort to lower symmetry. The low-dimensional character of this structure plays an important role in obtaining high critical temperatures in superconducting cuprates. The $A_2BO_{4+\delta}$ system (B = Cu,

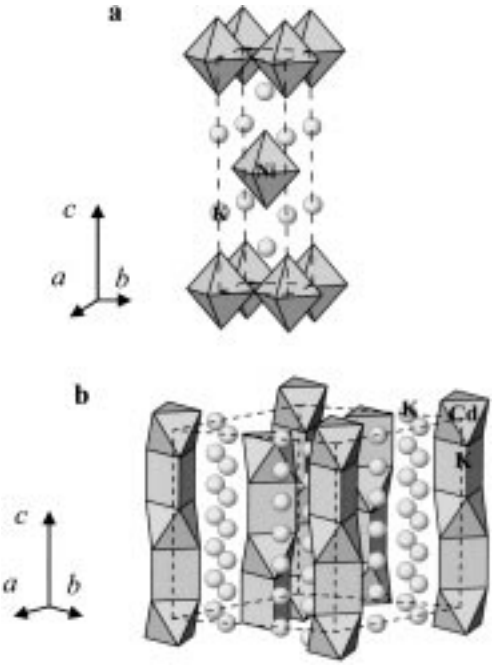

Figure 1. The structure of a) K_2NiF_4 and b) K_4CdCl_6.

[a] Prof. J. M. González-Calbet, Dr. A. Varela, Dr. K. Boulahya, Dr. M. Parras
Dpto. Química Inorgánica, Facultad de Ciencias Químicas
Universidad Complutense de Madrid, 28040 Madrid (Spain)
Fax: (+34) 91 3944352
E-mail: jgcalbet@eucmax.sim.ucm.es

[b] Dr. T. Vogt
Department of Physics, Brookhaven National Laboratory Upton
New York, 11973 (USA)

[c] Dr. A. Varela, Prof. D. J. Buttrey
Department of Chemical Engineering, University of Delaware
Newark, Delaware, 19716 (USA)

0947-6539/01/0707-1444 $ 17.50+.50/0

Ni)[1–4] has been extensively studied because of the critical dependence of transport and magnetic properties on the oxygen content. The ability of these B cations to adopt different coordination environments allows the formation of oxygen deficient K_2NiF_4-type structures in 3d transition metal oxides where single AO-type layers grow between single oxygen deficient perovskite layers, the oxygen vacancies being concentrated in the basal plane of the BO_6 octahedra.[5, 6]

Different behaviour is expected during the reduction of the 4d and 5d transition metal A_2BO_4 oxides. In such oxides, under low oxygen partial pressure (P_{O_2}), the B cation is not able to modify the octahedral oxygen environment. Therefore, anion-deficient $A_2BO_{4-\delta}$ materials cannot be stabilized. Jacob et al.[7] recently investigated the phase relation in the Sr–Ir–O system in order to design appropriate working electrodes for solid-state cells. As a function of P_{O_2}, they established different equilibria between several phases, such as $SrIrO_3$, Sr_2IrO_4 and Sr_4IrO_6. Particular attention was given to the reversible equilibrium between Sr_2IrO_4 and Sr_4IrO_6 since, at lower P_{O_2}, the layered material is dissociated into Sr_4IrO_6 and Ir metal. It is worth mentioning that, in all these oxides, Ir shows a 4+ oxidation state and an octahedral environment.

The Sr_4IrO_6 phase is isostructural to K_4CdCl_6[8] (Figure 1b). This structure, closely related to the 2H-hexagonal perovskite, can be described as formed by one Cd octahedra sharing faces with one K trigonal prism leading to isolated polyhedra chains parallel to the *c* axis, separated by K atoms. Between this and the 2H–$BaNiO_3$[9] structure, many intermediate phases have been reported belonging to the $(A_3B_2O_6)_\alpha(A_3B_3O_9)_\beta$ monodimensional oxides series.[10] Their structures are also formed by isolated chains of octahedra and trigonal prism alternating, in a variable ratio, along the *c* axis. The lower limit of this series corresponds to the $\alpha=\infty$, $\beta=0$ member of the monodimensional family $(A_3B_2O_6)_\alpha(A_3B_3O_9)_\beta$ and adopts the rhombohedral ($R\bar{3}c$) K_4CdCl_6 structure.

The dissociation process of the Sr_2IrO_4 (214) phase into the Sr_4IrO_6 (416) phase could be related to the impossibility of creating an anion deficiency in the layered phase. If this is true, this transformation could be a general way of accommodating the compositional changes in these A_2BO_4 phases. In order to establish if the (214) → (416) dissociation process is the general behaviour when the B cation is only stable in octahedral environment, we have investigated a system where both phases are stable: the Sr–Rh–O system. Actually, Rh shows a strong tendency to occupy octahedral environments and both layered Sr_2RhO_4[11–13] and monodimensional $Sr_3(SrRh)O_6$ (i.e., Sr_4RhO_6)[14] are stable phases which have been fully characterized.

This paper reports a study of the structural changes occurring during reduction of the $Sr_2RhO_{4+\delta}$ material. Our results reinforce the idea that the dissociation process of the layered (214) phase into the monodimensional (416) phase might be a general behaviour, in both 4d and 5d transition elements. From these results, the structural mechanism corresponding to such a transformation is proposed.

Abstract in Spanish: *Los cambios estructurales que acompañan al proceso de reducción de la fase $Sr_2RhO_{4+\delta}$ (214), término $n=1$ de la serie de Ruddlesden y Popper, muestran que, para valores de $\delta < 0.02$, esta fase se disocia dando lugar al compuesto monodimensional, Sr_4RhO_6 (416), término $\alpha=\infty$, $\beta=0$ de la familia $(A_3B_2O_6)_\alpha(A_3B_3O_9)_\beta$, y Rh metálico. En la primera etapa de este proceso de reducción se forma un intercrecimiento entre las fases (214) y (416), que sólo puede detectarse por HREM, y que se interpreta fácilmente si consideramos la relación estructural presente entre ambos materiales. Una reducción progresiva origina la segregación de las dos fases separadas que coexisten con Rh metálico. El proceso es reversible y, en atmósfera oxidante, se obtiene de nuevo la fase $Sr_2RhO_{4+\delta}$, con $\delta=0.06$. Esta disociación parece ser la forma general de acomodación de la variación de la composición en las fases A_2BO_4 en las que el catión B mantiene siempre su entorno octaédrico. En este trabajo se propone el mecanismo estructural por el que podría transcurrir esta transición y se establece la relación estructural presente entre estos dos óxidos de baja dimensionalidad.*

Results

XRD Study: The powder powder X-ray diffraction (XRD) pattern shown in Figure 2a corresponds to the $Sr_2RhO_{4.04}$ starting material. It can be indexed on the basis of a tetragonal $\sqrt{2}a \times 2c$ superstructure of the parent K_2NiF_4 cell, as early reported for ($I4_1/acd$) Sr_2RhO_4.[11–13] No structural changes are observed for the $Sr_2RhO_{4.02}$ composition. The unit cell parameters for both samples are shown in Table 1.

Table 1. Chemical composition, annealing conditions, identified phases and unit cell parameters for $Sr_2RhO_{4+\delta}$ materials.

Composition	Annealing conditions	Identified phases by XRD	Unit cell parameters		
			a [nm]	*b* [nm]	*c* [nm]
$Sr_2RhO_{4.04(1)}$	starting material	(214)	0.5451(2)		2.576(2)
$Sr_2RhO_{4.02(1)}$	900 °C (24 h) Ar atmosphere	(214)	0.5450(2)		2.576(1)
$Sr_2RhO_{3.98(1)}$	1000 °C (24 h) Ar atmosphere	(214) + (416) (traces)	0.383(4)	0.386(4)	1.29(1)
$Sr_2RhO_{4-\delta}$ (*)	1150 °C (24 h) Ar atmosphere	(416)+Rh			
$Sr_2RhO_{4.06(1)}$	1100 °C (72 h)/O_2 from (*) sample	(214)	0.54490(2)		2.5766(1)

The thermogravimetric analysis of the sample annealed under an Ar atmosphere at 1000 °C leads to an apparent composition $Sr_2RhO_{3.98}$. This sample shows meaningful differences in its XRD pattern (Figure 2b) when compared with the unannealed sample. Firstly, the (*hhl*) and (*hkl*) with $l=2n$ reflections of the starting material are split. Such a splitting could suggest a symmetry reduction, probably related to a tilt of the [RhO_6] octahedra. The origin of this distortion is beyond the scope of this study but, to take it into account, an orthorhombic unit cell with parameters $a=0.383$, $b=0.386$ and $c=1.29$ nm has been considered for this (214) phase. In addition to the reflections corresponding to such a phase, weak maxima appear which could correspond to the strongest reflexions of the rhombohedral (416) phase.

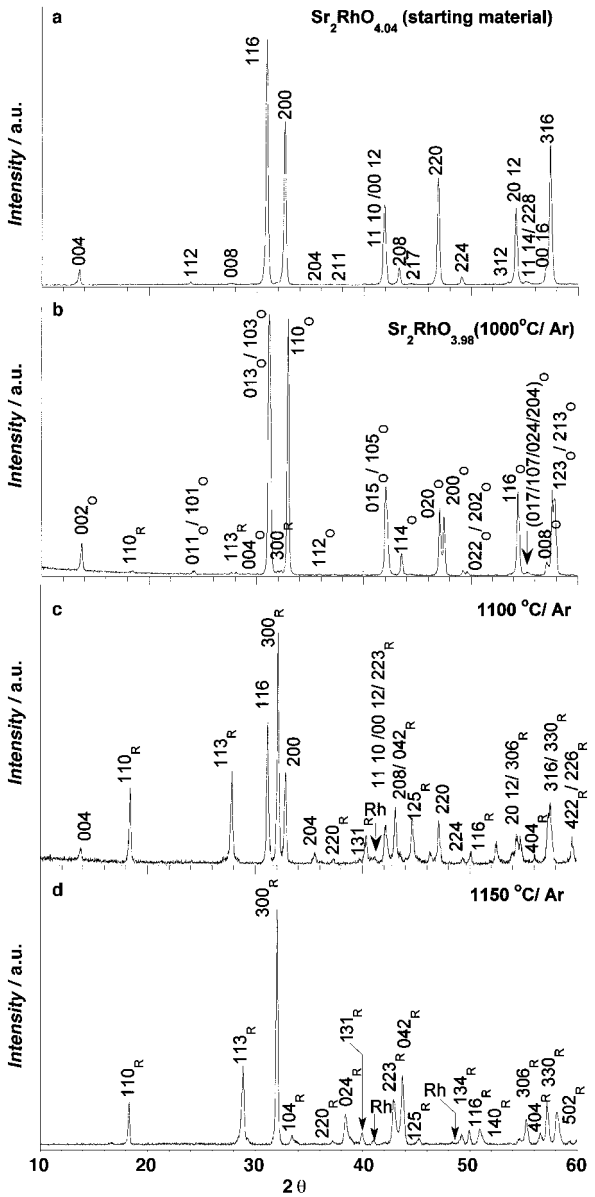

Figure 2. Powder X-ray diffraction patterns of a) $Sr_2RhO_{4.04}$ (starting material), b) sample with average composition $Sr_2RhO_{3.98}$ (subindex o and R correspond to the orthorhombic and the rhombohedral phases, respectively), c) sample annealed at $T = 1100\,^{\circ}C$ (Ar atmosphere), d) sample annealed at $T = 1150\,^{\circ}C$ (Ar atmosphere).

Several annealings at high temperature ($1000 \leq T \leq 1150\,^{\circ}C$) under an Ar atmosphere cause a progressive decomposition of the starting material. In this temperature range, the (214) phase coexists with Sr_4RhO_6 and Rh metal in a variable ratio. For instance, Figure 2c shows the XRD pattern corresponding to a sample treated at $1100\,^{\circ}C$ for 24 hours. When the temperature reaches $1150\,^{\circ}C$, only two phases, Sr_4RhO_6 and Rh, are present (Figure 2d). This decomposition reaction is a reversible process and a tetragonal $Sr_2RhO_{4.06}$ phase is always obtained from the reaction between Sr_4RhO_6 and Rh metal under oxidizing conditions. Unit cell parameters corresponding to this composition are also presented in Table 1.

Powder XRD data indicate that the stability range of the tetragonal $Sr_2RhO_{4+\delta}$ phase is very narrow ($0.02 \leq \delta \leq 0.06$). For δ values lower than 0.02, the (214)-type phase partially decomposes to rhombohedral Sr_4RhO_6. Both phases with Rh metal coexist in the temperature range from 1000 to $1150\,^{\circ}C$, the proportion of starting material decreasing as the temperature increases. At the upper temperature, the decomposition process is complete, the (214) phase not being detected by XRD.

SAED and HREM Characterization: Figure 3a shows the selected area electron diffraction (SAED) pattern characteristic of the sample with average composition $Sr_2RhO_{3.98}$ which

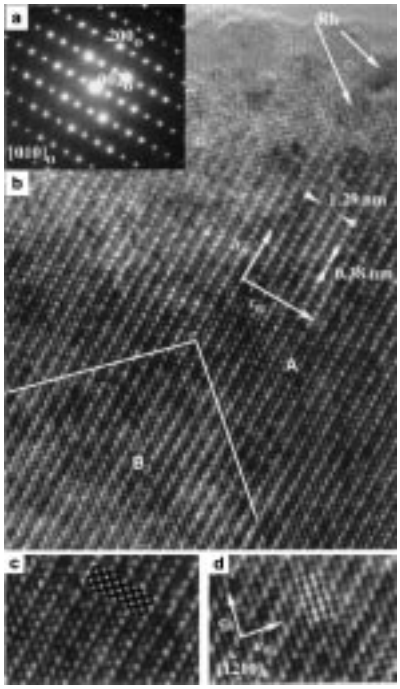

Figure 3. a) SAED pattern corresponding to the sample with average composition $Sr_2RhO_{3.98}$ along the $[010]_O$ zone axis. b) Corresponding HREM image. c) Enlargement of area A. Calculated image ($\Delta f = -65$ nm, $\Delta t = 4$ nm) is shown in the inset. d) Enlargement of area B. The image contrast is characteristic of a Sr_4RhO_6 phase along $[\bar{2}110]_R$. Calculated image ($\Delta f = -95$ nm, $\Delta t = 4.5$ nm) is shown in the inset.

corresponds to the [010] reciprocal plane of the K_2NiF_4 phase. All diffraction maxima have been indexed on the basis of the orthorhombic unit cell proposed from XRD results (referred to as subindex *o*). It is worth emphasizing that all crystals studied by SAED present the same features. Moreover, the corresponding high resolution electron microscopy (HREM) image (Figure 3b) shows an apparently well-ordered crystal where *d* spacings of 0.38 nm and 1.29 nm can be observed. These interplanar distances correspond to the d_{100} and d_{001} spacings of the orthorhombic (214) phase, respectively. In fact, most of the crystal shows a contrast variation (marked A) corresponding to a K_2NiF_4 structure projected along the $[010]_o$ zone axis. The alternation of one bright and one less bright dot following the $[301]_o$ direction is more clearly observed in Figure 3c (enlargement of area A in Figure 3b). This sequence, typical for the K_2NiF_4 structure, is due to the

0947-6539/01/0707-1446 $ 17.50+.50/0 *Chem. Eur. J.* **2001**, *7*, No. 7

alternance of one Sr and one Rh atom along such a direction. The simulated image (inset in Figure 3c) with $\Delta f = -65$ nm and sample thickness of 4 nm fits well to the experimental image.

However, careful examination of the micrograph indicates that in between the (214) phase, small regions showing different features are present. As it can be seen in the triangular marked area (zone B) of Figure 3b, the image contrast is slightly different than that observed in other parts of the crystal. In fact, following the $[301]_o$ direction, the 1:1 dot sequence characteristic of the (214) phase, changes to a 1:2:1:2 dot sequence in the zone B of the image. This sequence can be better observed in the enlargement of zone B shown in Figure 3d. This contrast variation, corresponding to two bright dots separated by one less intense dot, is characteristic of the rhombohedral $A_3(AB)O_6$ phase projected along $[1\bar{2}10]_R$. The individual columns of Sr and Rh atoms are solved as bright dots of different intensity. The brightest ones could be assimilated to Sr atoms, both in trigonal prismatic sites and between them, forming a rectangular array. The less intense dots are attributed to Rh octahedra. Similar features have been reported previously for the $Ca_3Co_2O_6$ isostructural phase.[15, 16] By this reasoning, the small domains shown in area B should correspond to the Sr_4RhO_6 phase. In fact, the simulated image (inset in Figure 3d) shows a good fit with the experimental image for $\Delta f = -95$ nm and a sample thickness of 4.5 nm. In this area, the observed *d* spacings close to 0.8 nm correspond to the d_{100} and d_{002} spacings of the rhombohedral phase. These distances remain almost constant within the crystal because they also correspond to three times the d_{103} and $d_{10\bar{3}}$ of the orthorhombic (214) phase. The c_R axis (subindex R refers to the Sr_4RhO_6 rhombohedral phase) appears elongated, probably due to a small distortion needed to facilitate the intergrowth of the rhombohedral phase into the orthorhombic (214) matrix. Such an intergrowth, schematically represented in Figure 4, takes place along the $[311]_o$ or $[001]_R$ directions, the a_R axis corresponding to the $[\bar{3}11]_O$ direction.

The cationic composition of the intergrown phases has been confirmed by energy dispersive spectroscopy (EDS). Figure 5 shows the analysis performed in different crystal zones. The major part of the crystal shows a Sr/Rh ratio of 2:1, characteristic of the K_2NiF_4 structure, but some areas present a 4:1 ratio, corresponding to the (416) phases. The HREM images also show the presence of dark sphere-like particles at the crystal surface which, according to EDS analysis, correspond to Rh particles.

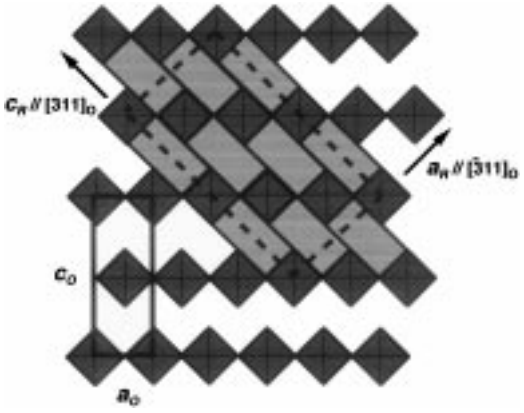

Figure 4. Schematic representation projected along $[001]_O//[010]_R$ of the intergrowth between (214) (unit cell denoted with a continuous border) and rhombohedral Sr_4RhO_6 (unit cell marked with a dashed border) structures.

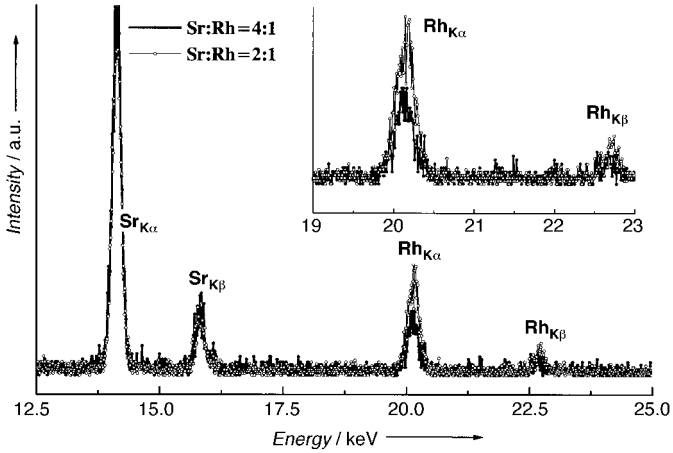

Figure 5. EDS spectra corresponding to different zones of the crystal shown in Figure 3b ($Rh_{K\alpha}$ line is shown in the inset).

The optical Fourier transform corresponding to areas A and B (Figures 6a and 6b) are identical. The similar features along both $[010]_O$ and $[1\bar{2}10]_R$ reciprocal planes can be visualized in the schematic representation of Figure 6c. Since all rhombohedral and orthorhombic diffraction maxima are coincident, the intergrowth cannot be detected by SAED.

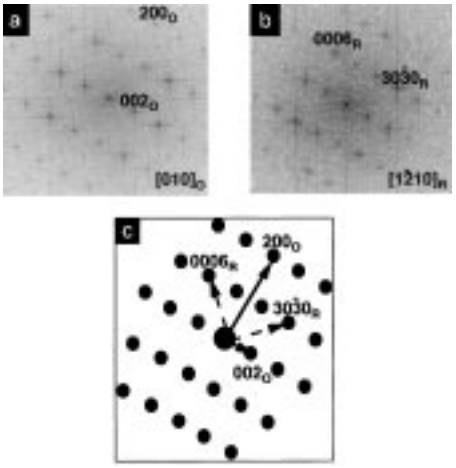

Figure 6. Fourier transform corresponding to a) area A and b) area B of the experimental micrograph shown in Figure 3b. c) Schematic representation of the SAED along $[010]_O$ //$[1\bar{2}10]_R$.

Annealing under lower P_{O_2} produces a progressive decomposition of the starting material leading to non-intergrowing phases: (214), (416) and Rh metal, according to the XRD results.

Discussion

XRD results show that under reducing thermodynamic conditions the layered $Sr_2RhO_{4+\delta}$ material decomposes and is partially transformed into the monodimensional Sr_4RhO_6. This transformation takes place according to the process $Sr_2RhO_4 \rightarrow Sr_4RhO_6 + Rh$ as a function of the partial oxygen pressure in agreement to the dissociation process described in the Sr–Ir–O system.[7] The microstructural information obtained from SAED, HREM and EDS can shed more light on the possible path by which this transformation occurs.

In the first stage, this process leads to the formation of nonrecurrent intergrowths between the orthorhombic (214) phase and the rhombohedral one. Therefore, both solids must present structural features which allow the rhombohedral phase to be transformed into a (214) matrix. Moreover, the fact that the transition between layered and monodimensional perovskite-related oxides is reversible seems to indicate that the mechanism for structural change is not complex and, therefore, a close relationship between both structures is expected.

In a previous work,[17] simple, novel models of crystallographic shear planes were proposed to interpret the structural relationships between several two-dimensional structures of oxides and fluorides. For instance, in relation to the K_2NiF_4 type, this model of extended planar defects allows correlation of the $Ba_4(Ti, Pt)_3O_{10}$ or $Cs_4Cu_3F_{10}$ structures with $Cs_6Ni_5F_{16}$. By means of a shear operation, octahedral sites are generated, which are occupied by transition metal atoms. This leads to an increase in the transition metal to alkaline metal ratio. Otherwise, the structural transformation from the A_2BO_4 composition into the $A_3(AB)O_6$ one must be accompanied by the elimination of B metal, thus leading to a decrease in the B/A ratio.

In order to understand the structural modifications involving the A_2BO_4 (K_2NiF_4 type) $\rightarrow A_3(AB)O_6$ (K_4CdCl_6 type) transformation, it is useful to consider the projection of the K_2NiF_4 structure along $[\bar{1}10]$ (Figure 7a). White octahedra (and shaded circles) are placed at $z = ½$ and shaded octahedra (and white circles) at $z = 0$. The transformation of the K_2NiF_4 structure into K_4CdCl_6 proceeds through the elimination of certain BO_6 octahedra. The supression of one every two (001) planes along the [110] direction leads to isolated octahedra in the ABO_3 perovskite layers, as shown in Figure 7b.

The essential feature of this elimination is that trigonal prismatic holes are generated along the $[311]_o$ and equivalent directions of the K_2NiF_4 structure. As a consequence, one trigonal prism and one octahedral site alternate in this direction. Tilting one of every two octahedra, together with a slight shifting of A atoms, as shown in Figure 7b, leads to the structural framework of the rhombohedral phase when regarded along the $[\bar{1}100]$ projection (Figure 7c).

On the other hand, it is known that the rhombohedral phase can be derived from a *hcp* stacking sequence of the $A_3A'O_6$ layers whereas the K_2NiF_4 structure can also be described as a cubic sequence of A_2O_4 layers.[17, 18] From this point of view, the above structural transformation implies that the A_2O_4 layers (stacked along the [311] and equivalent directions) have been reduced to A_4O_6 layers. Although the essential features of these layers are maintained, the anion composition has changed (Figures 8a, b).

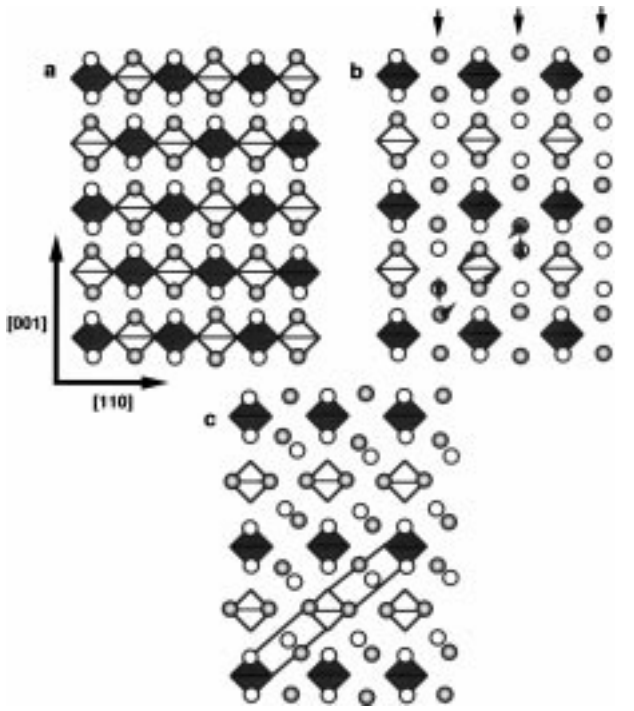

Figure 7. a) Schematic representation of the K_2NiF_4 structure along $[\bar{1}10]_O$. b) Isolated octahedra [RhO_6] and trigonal prismatic holes along $[311]_O$ and equivalent directions, resulting from the elimination of the RhO_2 planes marked with arrows. c) Structural framework of the Sr_4RhO_6 phase along the $[\bar{1}100]$ projection.

The rearrangement of A atoms (in A_4O_6 layers) takes place in such a way that one A atom is centering the triangle defined by three A atoms. In other words, it is at the center of the trigonal prism defined by the oxygen atoms of the adjacent layers. As a consequence, a rhombohedral A_3AO_6 layer is formed, as shown in Figure 8c. From these layers, the

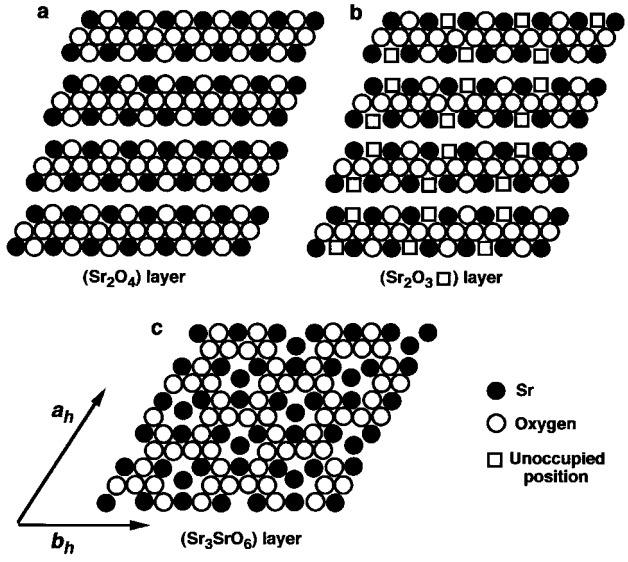

Figure 8. Idealized representation of the a) orthorhombic Sr_2O_4 layer, b) $Sr_2O_3\square$ layer and c) rhombohedral Sr_3SrO_6 layer.

0947-6539/01/0707-1448 $ 17.50+.50/0 *Chem. Eur. J.* **2001**, *7*, No. 7

$A_3(AB)O_6$ structure results when the octahedral holes are fully occupied by B cations.

According to these structural considerations, both *a* and *c* rhombohedral axes follow the $[311]_o$ and $[\bar{3}11]_o$ orthorhombic directions, respectively. From this relationship, the resulting *a* and *c* parameters are very close, 0.98 nm, in agreement with the typical values characteristic of $A_3(AB)O_6$ phases.

These structural data clearly show the close relationship between both K_2NiF_4- and K_4CdCl_6-type structures and provide a key for the understanding of the $Sr_2RhO_4 \rightarrow Sr_4RhO_6$ dissociation. Moreover, the adaptability of the A_2BO_4 structural type to accommodate the $A_3(AB)O_6$ rhombohedral framework is responsible for the occurrence of intergrowth domains in a variable extention. From a chemical point of view, the proposed structural mechanism could be considered as a reduction process according to the low P_{O_2} required to stabilize the Sr_4RhO_6 produced from the Sr_2RhO_4 material.

This behaviour is not necessarily limited to the $n=1$ member of the layered Ruddlesden and Popper phases. It seems reasonable to consider whether such a structural transformation between Sr_2RhO_4 and Sr_4RhO_6 can also take place between other members of both the layered and monodimensional series, and, consequently, if it is a factor affecting the thermodynamic stability of these materials. For instance, from the $Sr_3Rh_2O_7$ ($n=2$) member, a similar transformation mechanism could yield to the $Sr_5(SrRh_3)O_{12}$ monodimensional oxide ($\alpha=3, \beta=2$) and Rh metal. As yet, attempts to obtain the (327) layered phase have been unsuccessful, but new synthesis procedures, including high pressure methods, are being tested to explore such a possibility.

Conclusion

These experimental data show that, besides Ir, when Rh occupies the B positions in the A_2BO_4 layered phases the reduction process undergoes through a dissociation path corresponding to the reversible equilibrium $2Sr_2RhO_{4+\delta} \rightleftharpoons Sr_4RhO_6+Rh+(1+\delta)\ O_2$. Such a result reinforce the idea that it might be a general behaviour of the (214) phases when the B octahedral environment cannot be altered.

In the first stage of this transformation, intergrowths are formed between the orthorhombic (214) phase and the rhombohedral one, along the $[311]_o$ and $[\bar{3}11]_o$ directions of the layered phase. The similarity between both structures enables the formation of the rhombohedral phase into a (214) matrix providing a way to accommodate the compositional changes. Rh metal is excluded according to the structural mechanism proposed for this transformation. During the reduction process, the domain size of rhombohedral Sr_4RhO_6 increases until a critical strain buildup prevents further growth and phase separation occurs. The close structural relationships between both structural types facilitates the reversible transformation between them.

Experimental Section

$Sr_2RhO_{4.04}$ starting material has been prepared by solid-state reaction from stoichiometric amounts of $SrCO_3$ (Merck, 99.9%) and Rh_2O_3 (Aldrich, 99.8%). The mixture was initially heated in air at 1000 °C for several hours, then at 1150 °C for 7 h, and, finally, at 1250 °C for 50 h. A further annealing was performed at 900 °C under 1 bar oxygen. In order to obtain samples with different oxygen contents, the final product was annealed under the conditions given in Table 1.

The average cationic composition was determined by inductive coupling plasma (ICP). A 2:1 Sr/Rh ratio was always obtained. The cationic composition for every crystal, was determined by EDS. For this purpose, a JEOL scanning electron microscope JSM-8600 equipped with a LINK AN 10000 EDS system was employed. Thermogravimetric analysis was performed on a thermobalance based on a CAHN D-200 electrobalance which allows to detect variations of the oxygen content within $\pm 5 \times 10^{-3}$ on a sample of about 100 mg. The overall oxygen content was determined thermogravimetrically by reduction at 850 °C under a H_2 (0.3 mbar)/He (0.2 mbar) atmosphere, after which the final products of the reduction process are SrO and Rh.

XRD pattterns were collected at room temperature on a Philips X'Pert diffractometer using $Cu_{K\alpha}$ radiation. SAED was carried out using a JEOL 2000 FX electron microscope fitted with a double-tilting goniometer stage ($\pm 45°$) and HREM was performed on a JEOL 4000EX electron microscope fitted with a double-tilting goniometer stage ($\pm 25°$). Simulated HREM images were calculated by the multislice method using the MacTempas software package.

Acknowledgements

We acknowledge the financial support of CICYT (Spain) through Research Project MAT98–0648. A.V. acknowledges the Spanish Ministry of Education for a Posdoctoral fellowships.

[1] B. Dabrowski, J. D. Jorgensen, D. G. Hink, S. Pei, D. R. Richards, H. B. Vanfleet, D. L. Decker, *Physica C* **1989**, *162–164*, 99–100.
[2] D. E. Rice, D. Buttrey, *J. Solid State Chem.* **1993**, *105*, 197–209.
[3] J. D. Jorgensen, B. Dabrowski, S. Pei, D. R. Richards, D. G. Hinks, *Phys. Rev. B* **1989**, *40*, 2187–2199.
[4] J. Rodriguez-Carvajal, M. T. Fernández-Díaz, J. L. Martínez, *J. Phys. Condens. Matter* **1991**, *3*, 3215–3224.
[5] M. Medarde, J. Rodriguez-Carvajal, M. Vallet-Regí, J. M. González-Calbet, J. Alonso, *Phys. Rev. B* **1994**, *49*, 8591–8599.
[6] M. Medarde, J. Rodríguez-Carvajal, *Z. Phys. B* **1997**, *102*, 307–315.
[7] K. T. Jacob, T. H. Okabe, T. Uda, Y. Waseda, *J. Alloys Comp.* **1999**, *288*, 188–196.
[8] G. Bergerhoff, O. Schmitz-Dumont, *Z. Anorg. Allg. Chem.* **1956**, *284*, 10–14.
[9] J. J. Lander, *Acta Crystallogr.* **1951**, *4*, 148–156.
[10] K. Boulahya, M. Parras, J. M. Gonzalez-Calbet, *Chem. Mater.* **2000**, *12*, 25–32.
[11] M. A. Subramanian, M. K. Crawford, R. L. Harlow, T. Ami, J. A. Fernández-Baca, Z. R. Wang, D. C. Johnston, *Physica C* **1994**, *235–240*, 743–744.
[12] M. Itoh, T. Shimura, Y. Inaguma, Y. Morij, *J. Solid State Chem.* **1995**, *118*, 206–209.
[13] T. Vogt, D. J. Buttrey, *J. Solid State Chem.* **1996**, *123*, 186–189.
[14] J. F. Vente, J. K. Lear, P. D. Battle, *J. Mater. Chem.* **1995**, *5*, 1785–1789.
[15] H. Fjellvag, E. Gulbrandsen, S. Aasland, A. Olsen, B. Hauback, *J. Solid State Chem.* **1996**, *124*, 190–194.
[16] K. Boulahya, M. Parras, J. M. Gonzalez-Calbet, *J. Solid State Chem.* **1999**, *145*, 116–127.
[17] C. Dussarrat, F. Grasset, J. Darriet, *Eur. J. Solid State Inorg. Chem.* **1995**, *32*, 557–576
[18] J. Darriet, M. A. Subramanian, *J. Mater. Chem.* **1995**, *5*, 543–552.

Received: June 26, 2000 [F2565]